PHYSICAL REVIEW E **97**, 033307 (2018)

Regularized lattice Boltzmann model for immiscible two-phase flows with power-law rheology

Yan Ba,[1] Ningning Wang,[2] Haihu Liu,[2,*] Qiang Li,[1] and Guoqiang He[1]
[1]*School of Astronautics, Northwestern Polytechnical University, 127 West Youyi Road, Xi'an 710072, China*
[2]*School of Energy and Power Engineering, Xi'an Jiaotong University, 28 West Xianning Road, Xi'an 710049, China*

(Received 20 November 2017; published 13 March 2018)

In this work, a regularized lattice Boltzmann color-gradient model is developed for the simulation of immiscible two-phase flows with power-law rheology. This model is as simple as the Bhatnagar-Gross-Krook (BGK) color-gradient model except that an additional regularization step is introduced prior to the collision step. In the regularization step, the pseudo-inverse method is adopted as an alternative solution for the nonequilibrium part of the total distribution function, and it can be easily extended to other discrete velocity models no matter whether a forcing term is considered or not. The obtained expressions for the nonequilibrium part are merely related to macroscopic variables and velocity gradients that can be evaluated locally. Several numerical examples, including the single-phase and two-phase layered power-law fluid flows between two parallel plates, and the droplet deformation and breakup in a simple shear flow, are conducted to test the capability and accuracy of the proposed color-gradient model. Results show that the present model is more stable and accurate than the BGK color-gradient model for power-law fluids with a wide range of power-law indices. Compared to its multiple-relaxation-time counterpart, the present model can increase the computing efficiency by around 15%, while keeping the same accuracy and stability. Also, the present model is found to be capable of reasonably predicting the critical capillary number of droplet breakup.

DOI: 10.1103/PhysRevE.97.033307

I. INTRODUCTION

Numerical modeling and simulation of immiscible multiphase flows have attracted considerable attention for decades, as such flows are not only rich in fundamental fluid mechanics phenomena, but also present in numerous engineering and environmental applications [1–4]. Traditionally, multiphase flows are simulated by solving the macroscopic Navier-Stokes equations (NSEs) together with various approaches to track or capture the interface between different fluids. Among these approaches, the front-tracking method, volume-of-fluid (VOF) method, and level-set method are commonly used. While the front-tracking method is not suitable for simulating interface breakup and coalescence, the VOF and level-set methods require an interface reconstruction or reinitialization step to represent or correct the interface, which may be nonphysical or complex to implement. These disadvantages can be overcome by the lattice Boltzmann (LB) method, which tracks evolution of the distribution function of an assembly of molecules and is built upon microscopic models and mesoscopic kinetic equations [5]. The LB method has several advantages over traditional Navier-Stokes-based solvers, such as the algorithm simplicity and parallelizability, and the ease of handling complex boundaries [6]. In addition, its kinetic nature allows a simple incorporation of microscopic physics without suffering from the limitations in terms of length and time scales typical of molecular dynamics simulations. As such, the LB method is particularly useful in the simulation of multiphase, multicomponent flows. We refer the reader to Refs. [1,7–13] for a more detailed review.

The Bhatnagar-Gross-Krook (BGK) model [14,15] is the most widely used LB model for its algorithm simplicity and programming efficiency, which uses a single relaxation time in the collision operator. However, it suffers from poor numerical stability and low accuracy when the fluid viscosity is beyond a certain range [12]. As a remedy, several improved models have been proposed, including the multiple-relaxation-time (MRT) model [16–18], the entropic LB model [19–21], and the regularized lattice Boltzmann (RLB) model [22–24]. The MRT model improves numerical stability by relaxing the hydrodynamic and nonhydrodynamic moments with different relaxation times. Since matrix calculations are involved in collision step, this model requires more computational time than the BGK model, and also, there is no universal criteria for choosing the most stable and reliable set of relaxation times [25]. In the entropic LB model, the monotonicity of the H-function is ensured by solving the nonlinear equation of a corrective coefficient for the relaxation time. The entropic model has shown great boosts in numerical stability [26], but a considerable computational cost is required to solve the nonlinear equation, making the entropic model more computationally expensive, even when compared to the MRT model [27]. By contrast, the RLB model can enhance the stability while retaining the simplicity of the BGK model by introducing an algebraic regularization or precollision step prior to the collision step without any matrix calculations or solution of additional nonlinear equations. Latt and Chopard [22] pointed out that the key idea of the RLB model is to enforce symmetrical property by preserving only the first-order term in the nonequilibrium part of the distribution function [22].

---

*haihu.liu@xjtu.edu.cn

Zhang *et al.* [24] interpreted the regularization procedure in terms of the Hermite expansion and used the orthogonality relation between Hermite polynomials and Gauss-Hermite quadrature to reconstruct the nonequilibrium part such that the required nonequilibrium properties are preserved while filtering the undesirable high-order ghost (nonhydrodynamic) moments. Montessori *et al.* [25] recently showed that the regularization step can be loosely viewed as an equivalence to the early matrix LB schemes [28], where the hydrodynamic and ghost modes are relaxed at two different relaxation rates. As an analog to the MRT model, the RLB model has been demonstrated to substantially increase the stability and accuracy of LB simulations [25,27], indicating great potential in numerical investigation of various flow problems. Up to now, the study and applications of the RLB model have mostly been on single-phase flows [25,29–33], and the capability of the RLB model in multiphase flow simulations has been rarely examined except for the recent works by Otomo *et al.* [34,35], in which a RLB interparticle-potential model was developed to study two-phase displacement. However, their RLB interparticle-potential model may inherit some deficiencies of the original interparticle-potential model [7], e.g., the NSEs cannot be recovered exactly, and it suffers from poor numerical stability for moderate or large viscosity ratios [36]. Moreover, a dynamically changing viscosity has not yet been considered, which is inherent to non-Newtonian fluids frequently encountered in industry and daily life.

The aim of the present work is to develop a RLB version of the color-gradient model. In particular, we emphasize the capability of the model in dealing with power-law non-Newtonian rheology. Unlike Newtonian fluids, the viscosity of power-law fluids depends on the local shear rate, and often varies over a wide range especially for the fluids with moderate or strong rheological properties [32,37–39], posing a great challenge for LB models. It is therefore adopted for the examination of the present RLB model. Like the BGK color-gradient model [40,41], the present RLB model uses a forcing term to realize the interfacial tension effect and a recoloring algorithm to produce phase segregation. The Chapman-Enskog (C-E) multiscale analysis is first used to derive the constraint equations for the nonequilibrium part of total distribution function. We then propose to directly solve the constraint equations through the pseudo-inverse method, which does not need prior knowledge about the form of the nonequilibrium part and can be easily extended to other discrete velocity models. The resulting expressions for the nonequilibrium part are only related to macroscopic variables and velocity gradients that can be evaluated locally. Finally, the capability and accuracy of the present RLB model are tested by three typical numerical examples, including the single-phase and two-phase layered power-law fluid flows between two parallel plates, and the deformation and breakup of a Newtonian droplet immersed in a power-law matrix fluid subject to a simple shear flow.

II. NUMERICAL METHOD

A. RLB model for immiscible two-phase flows

The present LBM is developed based on the color-gradient model proposed by Halliday and his coworkers [40,41]. Distribution functions $f_{i,R}$ and $f_{i,B}$ are introduced to represent two immiscible fluids, red fluid and blue fluid, and the total distribution function is defined by $f_i = f_{i,R} + f_{i,B}$, where the subscript "i" denotes the ith direction of the lattice velocity, and the subscripts "R" and "B" refer to the red and blue fluids, respectively.

In each time step, the color-gradient model consists of three steps, i.e., the collision step, recoloring step, and streaming step. First, the total distribution function undergoes the collision step as

$$f_i^{\dagger}(\mathbf{x},t) = f_i(\mathbf{x},t) - \frac{1}{\tau}\left[f_i(\mathbf{x},t) - f_i^{\mathrm{eq}}(\mathbf{x},t)\right] + \hat{F}_i\delta_t, \qquad (1)$$

where the BGK approximation with a single relaxation time τ is used for the collision term; $f_i^{\dagger}(\mathbf{x},t)$ is the postcollision total distribution function at the position $\mathbf{x}$ and time ε, $\hat{F}_i$ is the forcing term, and δ_t is the time step. f_i^{eq} is the equilibrium distribution function of f_i is given by

$$f_i^{\mathrm{eq}} = \rho\omega_i\left[1 + \frac{\mathbf{e}_i\cdot\mathbf{u}}{c_s^2} + \frac{(\mathbf{e}_i\cdot\mathbf{u})^2}{2c_s^4} - \frac{\mathbf{u}^2}{2c_s^2}\right], \qquad (2)$$

where $\rho = \rho_R + \rho_B$ is the total density with ρ_R and ρ_B being the densities of red and blue fluids, respectively; $\mathbf{u}$ is the local fluid velocity; $c_s = c/\sqrt{3}$ is the speed of sound with $c = \delta_x/\delta_t$ being the lattice speed, in which δ_x is the lattice space (for the sake of simplicity, $\delta_x = \delta_t = 1$ is used hereafter); ω_i is the weight factor; and $\mathbf{e}_i$ is the lattice velocity vector in the ith direction. In this study, a two-dimensional (2D) nine-velocity model (D2Q9) and a three-dimensional (3D) 19-velocity model (D3Q19) are adopted for 2D and 3D simulations, respectively. For these two models, the lattice velocities and the weight factors are given as follows:

D2Q9:

$$[\mathbf{e}_0,\,\mathbf{e}_1,\cdots,\mathbf{e}_8] = \begin{bmatrix} 0 & 1 & 0 & -1 & 0 & 1 & -1 & -1 & 1 \\ 0 & 0 & 1 & 0 & -1 & 1 & 1 & -1 & -1 \end{bmatrix}, \qquad (3)$$

$$\omega_i = \begin{cases} 4/9, & i = 0; \\ 1/9, & i = 1,2,3,4; \\ 1/36, & i = 5,6,7,8. \end{cases} \qquad (4)$$

D3Q19:

$$[\mathbf{e}_0,\,\mathbf{e}_1,\cdots,\mathbf{e}_{18}] = \begin{bmatrix} 0 & 1 & -1 & 0 & 0 & 0 & 0 & 1 & -1 & 1 & -1 & 1 & -1 & 1 & -1 & 0 & 0 & 0 & 0 \\ 0 & 0 & 0 & 1 & -1 & 0 & 0 & 1 & 1 & -1 & -1 & 0 & 0 & 0 & 0 & 1 & -1 & 1 & -1 \\ 0 & 0 & 0 & 0 & 0 & 1 & -1 & 0 & 0 & 0 & 0 & 1 & 1 & -1 & -1 & 1 & 1 & -1 & -1 \end{bmatrix}, \qquad (5)$$

$$\omega_i = \begin{cases} 1/3, & i = 0; \\ 1/18, & i = 1,2,3,4,5,6; \\ 1/36, & i = 7,8,9,\dots,18. \end{cases} \tag{6}$$

The forcing term $\hat{F}_i$ in Eq. (1) contributes to the mixed interfacial region and creates an interfacial tension. According to Halliday *et al.* [41], the forcing term is given by

$$\hat{F}_i = \omega_i\left(1 - \frac{1}{2\tau}\right)\left[\frac{\mathbf{e}_i - \mathbf{u}}{c_s^2} + \frac{(\mathbf{e}_i\cdot\mathbf{u})\mathbf{e}_i}{c_s^4}\right]\cdot\mathbf{F}, \tag{7}$$

where the interfacial tension force $\mathbf{F}$ is introduced based on the continuum surface force method [42] and is expressed as

$$\mathbf{F}(\mathbf{x},t) = -\tfrac{1}{2}\sigma\kappa\nabla\rho^N, \tag{8}$$

where σ is an interfacial tension parameter. ρ^N is the color indicator defined by

$$\rho^N(\mathbf{x},t) = \frac{\rho_R(\mathbf{x},t) - \rho_B(\mathbf{x},t)}{\rho_R(\mathbf{x},t) + \rho_B(\mathbf{x},t)}, \quad -1 \leqslant \rho^N \leqslant 1, \tag{9}$$

and κ is the local interface curvature, which is expressed as

$$\kappa = -\nabla_S\cdot\mathbf{n} = -[(\mathbf{I} - \mathbf{n}\otimes\mathbf{n})\cdot\nabla]\cdot\mathbf{n}, \tag{10}$$

where $\mathbf{n}$ is the interfacial unit normal vector defined by $\mathbf{n} = -\nabla\rho^N/|\nabla\rho^N|$. Then the local fluid velocity is calculated by [43]

$$\rho\mathbf{u}(\mathbf{x},t) = \sum_i f_i(\mathbf{x},t)\mathbf{e}_i + \frac{1}{2}\mathbf{F}(\mathbf{x},t)\delta_t. \tag{11}$$

Using the C-E expansion, Eq. (1) can be reduced to the NSEs in the low-frequency, long-wavelength limit with Eqs. (2) and (7). The resulting equations are

$$\frac{\partial\rho}{\partial t} + \nabla\cdot(\rho\mathbf{u}) = 0, \tag{12a}$$

$$\frac{\partial\rho\mathbf{u}}{\partial t} + \nabla\cdot(\rho\mathbf{u}\mathbf{u}) = -\nabla p + \nabla\cdot[\mu(\nabla\mathbf{u} + \nabla\mathbf{u}^T)] + \mathbf{F}, \tag{12b}$$

where $p = \rho c_s^2$ is the pressure, and $\mu = \rho c_s^2\delta_t(\tau - 0.5)$ is the dynamic viscosity of the fluid mixture. In this work, the pure red and blue fluids are assumed to have equal densities: $\tilde{\rho}_R = \tilde{\rho}_B$. To account for unequal viscosities of both fluids, a harmonic mean is utilized for the viscosity of fluid mixture [44,45]:

$$\frac{1}{\mu(\rho^N)} = \frac{1 + \rho^N}{2\mu_R} + \frac{1 - \rho^N}{2\mu_B}, \tag{13}$$

where μ_k ($k = R$ or B) is the dynamic viscosity of fluid k.

To keep a sharp interface and produce phase segregation, the recoloring step is then applied. Compared to the original recoloring algorithm of Gunstensen *et al.* [46], the recoloring algorithm proposed by Latva-Kokko and Rothman [47] is known to reduce spurious velocities at the interface and overcome the lattice pinning problem. Following Ref. [47], the recolored distribution functions of red and blue fluids are given by

$$f_{i,R}^{\dagger\dagger}(\mathbf{x},t) = \frac{\rho_R}{\rho}f_i^{\dagger}(\mathbf{x},t) + \beta\frac{\rho_R\rho_B}{\rho}\omega_i\frac{\mathbf{e}_i\cdot\nabla\rho^N}{|\nabla\rho^N|},$$

$$f_{i,B}^{\dagger\dagger}(\mathbf{x},t) = \frac{\rho_B}{\rho}f_i^{\dagger}(\mathbf{x},t) - \beta\frac{\rho_R\rho_B}{\rho}\omega_i\frac{\mathbf{e}_i\cdot\nabla\rho^N}{|\nabla\rho^N|}, \tag{14}$$

where $f_{i,R}^{\dagger\dagger}(\mathbf{x},t)$ and $f_{i,B}^{\dagger\dagger}(\mathbf{x},t)$ are the recolored distribution functions of red and blue fluids, respectively, and β is a segregation parameter related to the interface thickness. In the present work, β is chosen as 0.7 to maintain a narrow interface thickness (around four or five lattices) and keep spurious velocities at a low level [41,44]. In addition, Liu *et al.* [48] indicated that such a choice is necessary to reproduce correct interface behavior.

After the recoloring step, the streaming step for both red and blue distribution functions is performed:

$$f_{i,k}(\mathbf{x} + \mathbf{e}_i\delta_t, t + \delta_t) = f_{i,k}^{\dagger\dagger}(\mathbf{x},t), \quad k = R \text{ or } B. \tag{15}$$

With the poststreaming distribution functions, the density of each fluid is calculated by

$$\rho_k = \sum_i f_{i,k}, \quad k = R \text{ or } B. \tag{16}$$

It is known that the standard BGK model has been successfully applied to the simulation of non-Newtonian fluid flows, but it is often restricted to a small range of dynamic viscosities because of low numerical accuracy or instability. To allow for the power-law fluids with moderate or strong rheological properties in which the viscosities often vary within a wide range, we propose to use a RLB model instead of the standard BGK model. The RLB model is as simple as the BGK model except that an additional regularization step is applied prior to the collision step; see Eq. (1). In the regularization step, the total distribution function is divided into an equilibrium part f_i^{eq} and a nonequilibrium part f_i^{neq}, and the nonequilibrium part is then approximated by the first-order term of f_i in the C-E expansion [22]. This means

$$f_i(\mathbf{x},t) = f_i^{\mathrm{eq}}(\mathbf{x},t) + f_i^{(1)}(\mathbf{x},t)\delta_t, \tag{17}$$

where $f_i^{(1)}$ is the nonequilibrium part of the first order in the C-E expansion.

Substituting the regularization step into Eq. (1), the evolution equation for the collision step reads as

$$f_i^{\dagger}(\mathbf{x},t) = f_i^{\mathrm{eq}}(\mathbf{x},t) + \left(1 - \frac{1}{\tau}\right)f_i^{(1)}(\mathbf{x},t)\delta_t + \hat{F}_i\delta_t. \tag{18}$$

It can be shown using the C-E expansion (see Appendix A) that Eq. (18) can recover the target NSEs [see Eq. (12)] if $f_i^{(1)}$ satisfies the following constraints:

$$\sum_i f_i^{(1)} = 0, \tag{19a}$$

$$\sum_i e_{i\alpha}f_i^{(1)} = -\frac{1}{2}F_\alpha, \tag{19b}$$

$$\sum_i e_{i\alpha}e_{i\beta}f_i^{(1)} = \eta S_{\alpha\beta}, \tag{19c}$$

with $\eta = -2\tau\rho c_s^2$ and

$$S_{\alpha\beta} = [(\partial_\alpha u_\beta + \partial_\beta u_\alpha)/2] + \left[(u_\alpha F_\beta + u_\beta F_\alpha)/4\tau\rho c_s^2\right], \tag{20}$$

where the subscripts α and β denote the coordinate directions. It can be seen from Eq. (19) that the number of unknown $f_i^{(1)}$ is more than the number of known constraint equations, which are 9 (or 19) and 6 (or 10), respectively, for the D2Q9 (or D3Q19) model. The problem of solving for $f_i^{(1)}$ in Eq. (19) is underdetermined and has many possible solutions. In previous studies, the expressions of $f_i^{(1)}$ were usually constructed by the C-E expansion or the Hermite expansion [22,24,29,32,49]. Here we propose to directly solve Eq. (19) for $f_i^{(1)}$ by using the pseudo-inverse method [50,51], which is based on a philosophy that the norm of solution is made minimum. The pseudo-inverse method is particularly suitable to find an optimum solution to the underdetermined equations, e.g., Eq. (19). With the pseudo-inverse method, one can obtain the analytical expressions of $f_i^{(1)}$ which are given by (see Appendix B for the derivation)

$$\begin{pmatrix} f_0^{(1)} \\ f_1^{(1)} \\ f_2^{(1)} \\ f_3^{(1)} \\ f_4^{(1)} \\ f_5^{(1)} \\ f_6^{(1)} \\ f_7^{(1)} \\ f_8^{(1)} \end{pmatrix} = \frac{1}{36} \begin{pmatrix} 0 & 0 & -12 & 0 & -12 \\ -3 & 0 & 6 & 0 & -12 \\ 0 & -3 & -12 & 0 & 6 \\ 3 & 0 & 6 & 0 & -12 \\ 0 & 3 & -12 & 0 & 6 \\ -3 & -3 & 6 & 9 & 6 \\ 3 & -3 & 6 & -9 & 6 \\ 3 & 3 & 6 & 9 & 6 \\ -3 & 3 & 6 & -9 & 6 \end{pmatrix} \begin{pmatrix} F_x \\ F_y \\ \eta S_{xx} \\ \eta S_{xy} \\ \eta S_{yy} \end{pmatrix}, \tag{21}$$

for the D2Q9 model and

$$\begin{pmatrix} f_0^{(1)} \\ f_1^{(1)} \\ f_2^{(1)} \\ f_3^{(1)} \\ f_4^{(1)} \\ f_5^{(1)} \\ f_6^{(1)} \\ f_7^{(1)} \\ f_8^{(1)} \\ f_9^{(1)} \\ f_{10}^{(1)} \\ f_{11}^{(1)} \\ f_{12}^{(1)} \\ f_{13}^{(1)} \\ f_{14}^{(1)} \\ f_{15}^{(1)} \\ f_{16}^{(1)} \\ f_{17}^{(1)} \\ f_{18}^{(1)} \end{pmatrix} = \frac{1}{420} \begin{pmatrix} 0 & 0 & 0 & -100 & 0 & 0 & -100 & 0 & -100 \\ -21 & 0 & 0 & 10 & 0 & 0 & -60 & 0 & -60 \\ 21 & 0 & 0 & 10 & 0 & 0 & -60 & 0 & -60 \\ 0 & -21 & 0 & -60 & 0 & 0 & 10 & 0 & -60 \\ 0 & 21 & 0 & -60 & 0 & 0 & 10 & 0 & -60 \\ 0 & 0 & -21 & -60 & 0 & 0 & -60 & 0 & 10 \\ 0 & 0 & 21 & -60 & 0 & 0 & -60 & 0 & 10 \\ -21 & -21 & 0 & 50 & 105 & 0 & 50 & 0 & -20 \\ 21 & -21 & 0 & 50 & -105 & 0 & 50 & 0 & -20 \\ -21 & 21 & 0 & 50 & -105 & 0 & 50 & 0 & -20 \\ 21 & 21 & 0 & 50 & 105 & 0 & 50 & 0 & -20 \\ -21 & 0 & -21 & 50 & 0 & 105 & -20 & 0 & 50 \\ 21 & 0 & -21 & 50 & 0 & -105 & -20 & 0 & 50 \\ -21 & 0 & 21 & 50 & 0 & -105 & -20 & 0 & 50 \\ 21 & 0 & 21 & 50 & 0 & 105 & -20 & 0 & 50 \\ 0 & -21 & -21 & -20 & 0 & 0 & 50 & 105 & 50 \\ 0 & 21 & -21 & -20 & 0 & 0 & 50 & -105 & 50 \\ 0 & -21 & 21 & -20 & 0 & 0 & 50 & -105 & 50 \\ 0 & 21 & 21 & -20 & 0 & 0 & 50 & 105 & 50 \end{pmatrix} \begin{pmatrix} F_x \\ F_y \\ F_z \\ \eta S_{xx} \\ \eta S_{xy} \\ \eta S_{xz} \\ \eta S_{yy} \\ \eta S_{yz} \\ \eta S_{zz} \end{pmatrix}, \tag{22}$$

for the D3Q19 model. In Eqs. (21) and (22), the second-order tensor $S_{\alpha\beta}$ can be calculated locally from the nonequilibrium part of the distribution function [see Eq. (19c)],

$$S_{\alpha\beta} = \frac{1}{\eta}\sum_i e_{i\alpha}e_{i\beta}f_i^{(1)} = \frac{1}{\eta}\sum_i e_{i\alpha}e_{i\beta}\left(f_i - f_i^{\mathrm{eq}}\right), \tag{23}$$

which can avoid the evaluation of the derivatives through the finite difference approximation and thus is more consistent with the philosophy of the LBM. As can be seen from Eqs. (21) and (22), the body force term is explicitly included in $f_i^{(1)}$, which suggests that a direct use of the previously proposed $f_i^{(1)}$ [22],

$$f_i^{(1)} = \frac{\omega_i}{2c_s^4}\left(e_{i\alpha}e_{i\beta} - c_s^2\delta_{\alpha\beta}\right)\sum_i e_{i\alpha}e_{i\beta}\left(f_i - f_i^{\mathrm{eq}}\right), \tag{24}$$

is invalid when the body force is taken into account. In addition, the pseudo-inverse method is directly applied for the solution of $f_i^{(1)}$, which does not need *a priori* knowledge regarding the form of $f_i^{(1)}$ and can be straightforwardly extended to other discrete velocity models. Finally, it is worth noting that the regularization step that neglects high-order terms in f_i^{neq} can ensure the symmetry of distribution function with respect to spatial reflection, thus improving the stability and accuracy of numerical simulations.

B. Modeling of power-law non-Newtonian fluid

For the power-law non-Newtonian fluid, the dynamic viscosity is not a constant but a function of the shear rate $|\dot{\gamma}|$, and is given by

$$\mu = \mu^p |\dot{\gamma}|^{n-1}, \tag{25}$$

where $\dot{\gamma}$ is the shear rate tensor defined by $\dot{\gamma} = \nabla\mathbf{u} + (\nabla\mathbf{u})^T$ and $|\dot{\gamma}| = \sqrt{(\dot{\gamma} : \dot{\gamma})/2}$; μ^p and n are the consistency constant and the power-law index, respectively. Depending on the value of n, the power-law fluids can be divided into three types: the shear-thinning or pseudo-plastic fluid for $n < 1$, the Newtonian fluid for $n = 1$, and the shear-thickening or dilatant fluid for $n > 1$. Note that, as a part of $S_{\alpha\beta}$, the local shear rate tensor $\dot{\gamma}$ involved in the viscosity calculation of the power-law fluid can be simply calculated by Eq. (20) once the value of $S_{\alpha\beta}$ is obtained from Eq. (23). With the local shear rate tensor, the relaxation time τ in Eq. (1) is calculated in the following way: μ_R and μ_B are first calculated by Eq. (25), the viscosity μ of the fluid mixture is then calculated by Eq. (13), and finally τ is obtained from $\mu = \rho c_s^2 \delta_t(\tau - 0.5)$, which is shown below Eq. (12).

III. RESULTS AND DISCUSSION

A. Single-phase power-law fluid flows between two parallel plates

To test the stability and accuracy of the present model, the benchmark case regarding a single-phase power-law fluid flow between two parallel plates is first considered. The flow is driven by a constant pressure gradient in the x direction, $\partial p/\partial x = -1.5 \times 10^{-7}$, and the channel has a height of H in the y direction. When the flow reaches the steady state, an analytical solution for the x component of the velocity can be obtained as [52]

$$u_x^*(y) = \frac{n}{1+n}\left(-\frac{1}{\mu^p}\frac{\partial p}{\partial x}\right)^{\frac{1}{n}}\left[\left(\frac{H}{2}\right)^{\frac{1+n}{n}} - \left|y - \frac{H}{2}\right|^{\frac{1+n}{n}}\right], \quad y \in [0,H], \tag{26}$$

from which the maximum velocity $u_{x,\max}^*$ is easily calculated:

$$u_{x,\max}^* = \frac{n}{1+n}\left(-\frac{1}{\mu^p}\frac{\partial p}{\partial x}\right)^{\frac{1}{n}}\left(\frac{H}{2}\right)^{\frac{1+n}{n}}. \tag{27}$$

The simulations are run in a 10×40 lattice domain. Periodic boundary conditions are applied in the x direction, while no-slip boundary conditions, which are realized by the half-way bounce-back rule, are used on the top and bottom walls. A broad range of power-law indices are considered: $n = 0.1, 0.2, 0.5, 1, 1.5$, and 2. In the simulations, μ^p is an adjustable parameter varying with n, and it is selected such that the analytical value of $u_{x,\max}^*$ given by Eq. (27) is fixed at 1×10^{-3} in order to minimize the compressibility errors. The convergence criterion is selected as

$$E_c = \frac{\sum_{\mathbf{x}} \|\mathbf{u}(\mathbf{x},t) - \mathbf{u}(\mathbf{x},t-100\delta_t)\|}{\sum_{\mathbf{x}} \|\mathbf{u}(\mathbf{x},t)\|} < 10^{-8}. \tag{28}$$

TABLE I. Relative errors of the velocity obtained by using the BGK and RLB models at different values of n in the single-phase power-law fluid flows.

n	E_u-BGK	E_u-RLB
0.1	Not converged	1.524×10^{-2}
0.2	Not converged	5.112×10^{-3}
0.5	1.562×10^{-3}	1.495×10^{-3}
1	8.193×10^{-4}	7.223×10^{-4}
1.5	6.496×10^{-4}	5.515×10^{-4}
2	5.864×10^{-4}	4.949×10^{-4}

To quantify the accuracy of the simulated results, we compute the relative L^2-norm error of the velocity in the steady state. The relative error is defined as $E_u = \sqrt{\sum_y [u_x(y) - u_x^*(y)]^2 / \sum_y [u_x^*(y)]^2}$, where u_x is the x component of the simulated velocity. Table I shows the relative errors of the velocity at different values of n, where the results obtained by the BGK model are also illustrated for comparison with the present RLB results.

It is found that all the simulations reach the steady state when the RLB model is used, but the simulations with $n \leqslant 0.2$ cannot converge when the BGK model is used, because in the central part of the channel, the velocity distribution is extremely even for a low power-law index, which could lead to very high viscosities, thus deteriorating the stability or accuracy of the BGK model. In addition, the simulated results from the RLB model all agree well with the analytical solutions with the relative errors below 1.524×10^{-2}. For the power-law indices above 0.5, the relative errors obtained by using the RLB and BGK models are on the same order of 10^{-3} or even smaller. These results indicate that the proposed RLB model can offer substantial improvements in stability over the BGK model and it is eligible in the simulation of power-law fluid flows with a wide range of power-law indices.

It should also be noted that for $n \leqslant 0.2$, the relative errors are higher because the macroscopic quantities, e.g., the velocity and viscosity, vary dramatically either in a thin layer or over an extremely wide range. It is expected that the accuracy of the simulated results can be improved by increasing grid resolution. Table II shows the relative errors of the velocity obtained by the RLB model for three different grid resolutions at $n = 0.1$ and $n = 0.2$. As expected, the relative errors are effectively reduced with increasing the grid number.

B. Two-phase power-law fluid flows between two parallel plates

To assess the capability of the present model in describing two-phase interface and dealing with different viscosities of the

TABLE II. Relative errors of the velocity obtained by the RLB model at $n = 0.1$ and $n = 0.2$ for different grid resolutions.

	E_u-RLB	
Grid resolution	$n = 0.1$	$n = 0.2$
$X \times Y = 10 \times 40$	1.524×10^{-2}	5.112×10^{-3}
$X \times Y = 20 \times 80$	3.698×10^{-3}	1.149×10^{-3}
$X \times Y = 30 \times 120$	1.538×10^{-3}	4.088×10^{-4}

binary fluids, we simulate the two-phase power-law fluid flows between two parallel plates. As shown in Fig. 1, two plates are apart from each other by a distance of $2H$ in the y direction. The red and blue fluids fill the central ($|y| \leqslant Y_i$) and bilateral ($Y_i < |y| \leqslant H$) regions of the channel, respectively. The lattice domain is set to be 5×200 with $Y_i = 50$. The flow is driven by a constant pressure gradient of $-\partial p/\partial x = 2.0 \times 10^{-8}$, and all the boundary conditions are the same as those in the above single-phase flow simulations.

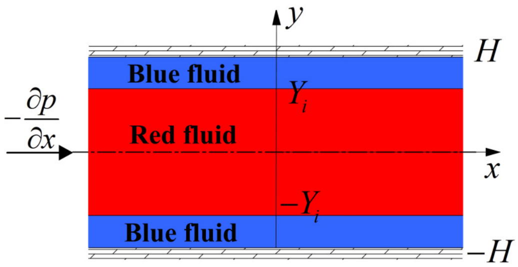

FIG. 1. Schematic of the two-phase layered flow between two parallel plates.

When the flow reaches the steady state, an analytical solution for the x component of the velocity is given by [39]

$$u_x^*(y) = \begin{cases} \frac{n_R}{1+n_R}\left(-\frac{1}{\mu_R^p}\frac{\partial p}{\partial x}\right)^{\frac{1}{n_R}}\left(Y_i^{\frac{1+n_R}{n_R}} - |y|^{\frac{1+n_R}{n_R}}\right) + \frac{n_B}{1+n_B}\left(-\frac{1}{\mu_B^p}\frac{\partial p}{\partial x}\right)^{\frac{1}{n_B}}\left(H^{\frac{1+n_B}{n_B}} - Y_i^{\frac{1+n_B}{n_B}}\right), & \text{if} \quad |y| \leqslant Y_i; \\ \frac{n_B}{1+n_B}\left(-\frac{1}{\mu_B^p}\frac{\partial p}{\partial x}\right)^{\frac{1}{n_B}}\left(H^{\frac{1+n_B}{n_B}} - |y|^{\frac{1+n_B}{n_B}}\right), & \text{otherwise,} \end{cases} \tag{29}$$

where n_R and n_B are the power-law indices of the red and blue fluids, respectively.

To consider different viscosities of the binary fluids, a parameter λ^p is introduced, which is defined by the consistency constants of both power-law fluids as $\lambda^p = \mu_R^p/\mu_B^p$. Different values of λ^p are obtained by varying μ_R^p while keeping μ_B^p fixed. The interfacial tension is fixed at $\sigma = 5 \times 10^{-3}$. Simulations are carried out at $\lambda^p = 0.1, 1$, and 10 for (a) $n_R = 0.2$, $n_B = 1$, (b) $n_R = 1.8$, $n_B = 1$, (c) $n_R = 0.2$, $n_B = 1.8$, and (d) $n_R = 1.8$, $n_B = 0.2$. Table III shows the relative errors of the simulated results obtained with the present RLB model and the BGK model.

Similar to the observations in the single-phase flow simulations, when the RLB model is used, all the simulations can converge and the simulated results show an acceptable accuracy with the relative errors on the order of 10^{-2} or even smaller. By contrast, the BGK simulations become unstable as long as there exists a shear-thinning fluid in binary fluids. In addition, the relative errors are found to be almost independent of the value of λ^p for each group of n_R and n_B, because the analytical velocity profiles are almost identical at different λ^p for the constant values of n_R and n_B, which can be seen from Fig. 2. As a comparison, Fig. 2 also plots the simulated results by the RLB model. Note that in each case the velocities and position are normalized by the maximum analytical velocity $u_{\max}^*$ and the half channel height H, respectively. A good agreement between the simulated and analytical results is observed for all the cases considered. Again, we find that the relative errors can be reduced by increasing grid resolution. For example, in the case of $\lambda^p = 1$, $n_R = 1.8$, and $n_B = 0.2$, the relative errors of the velocity are, respectively, 3.69×10^{-2}, 1.81×10^{-2}, and 1.09×10^{-2} for the grid resolutions of 4×200, 8×400, and 12×600; and in the case of $\lambda^p = 1$, $n_R = 0.2$, and $n_B = 1.8$, the relative errors are, respectively, 1.01×10^{-2}, 5.02×10^{-3}, and 2.53×10^{-3} for the grid resolutions of 4×200, 8×400, and 12×600.

TABLE III. Relative errors of the velocity obtained with BGK and RLB models for different flow conditions in the two-phase layered power-law fluid flows. Note that the parameter λ^p is defined as $\lambda^p = \mu_R^p/\mu_B^p$.

λ^p	n_R	n_B	E_u-BGK	E_u-RLB
0.1	0.2	1	Not converged	7.62×10^{-4}
1	0.2	1	Not converged	7.63×10^{-4}
10	0.2	1	Not converged	7.94×10^{-4}
0.1	1.8	1	3.66×10^{-2}	3.66×10^{-2}
1	1.8	1	3.59×10^{-2}	3.59×10^{-2}
10	1.8	1	2.91×10^{-2}	2.90×10^{-2}
0.1	0.2	1.8	Not converged	1.01×10^{-2}
1	0.2	1.8	Not converged	1.01×10^{-2}
10	0.2	1.8	Not converged	1.00×10^{-2}
0.1	1.8	0.2	Not converged	3.69×10^{-2}
1	1.8	0.2	Not converged	3.69×10^{-2}
10	1.8	0.2	Not converged	3.69×10^{-2}

C. Droplet deformation and breakup in a power-law shear flow

To validate the RLB model in capturing the dynamic interface, in particular with topological changes, we simulate the droplet deformation and breakup in a power-law shear flow, and the simulated results and the computing time are quantitatively compared with those obtained by the MRT model, which is known to have better stability and accuracy over the BGK model as well. As illustrated in Fig. 3, a spherical droplet with radius R is initially placed in the middle of two parallel plates. The two plates are apart from each other by a distance of H and move at an equal speed of U but in opposite directions. The resulting shear rate is $\dot{\gamma}_0 = 2U/H$, and the wall confinement is defined as $2R/H$. In what follows, we use the subscripts "R" and "B" to denote the droplet and the matrix fluid, respectively. When the droplet is subject to a simple shear flow, two primary forces, the capillary and viscous forces, are exerted on the droplet, and their relative magnitude is measured by the capillary number, which is defined by $\text{Ca} = \mu_B \dot{\gamma}_0 R/\sigma$. In addition, the inertial force can also influence the dynamical behavior of the droplet, and its importance is described by the Reynolds number, defined by $\text{Re} = \rho_B \dot{\gamma}_0 R^2/\mu_B$.

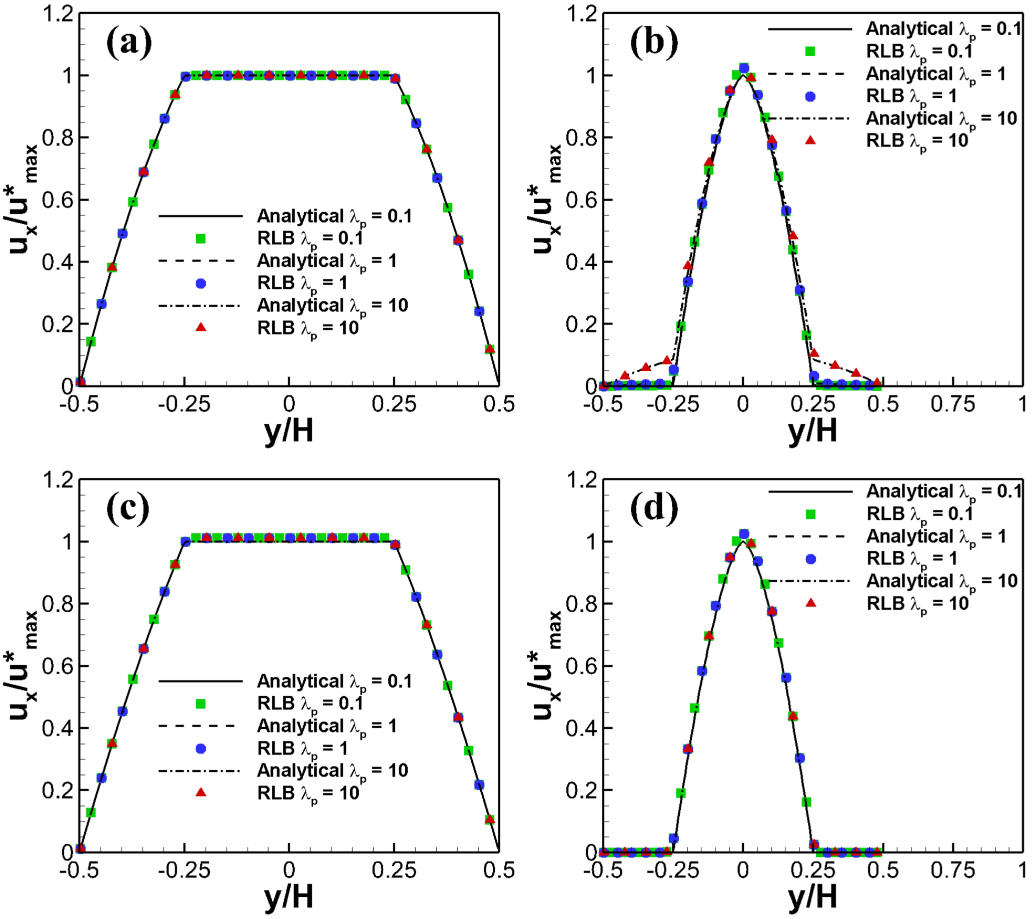

FIG. 2. Simulated and analytical velocity profiles at $\lambda^p = 0.1, 1$, and 10 for four different groups of n_R and n_B: (a) $n_R = 0.2$, $n_B = 1$, (b) $n_R = 1.8$, $n_B = 1$, (c) $n_R = 0.2$, $n_B = 1.8$, and (d) $n_R = 1.8$, $n_B = 0.2$. The simulated results from the RLB model and analytical solutions are represented by the discrete symbols and lines, respectively. Note that in each case the velocities and position are normalized by the maximum analytical velocity $u^*_{\max}$ and the half channel height H, respectively.

Previous works have indicated [39,53,54] that the non-Newtonian rheology of the matrix fluid has a more significant effect on the droplet behavior than that of the droplet. Thus, we will focus on the fluid systems with a Newtonian droplet suspended in a power-law matrix. According to Eq. (25), the viscosity of the matrix fluid in the definitions of Ca and Re is given by $\mu_B = \mu_B^p|\dot{\gamma}|^{n_B-1}$ with $|\dot{\gamma}| = \dot{\gamma}_0$ as an estimate. In the present study, three typical power-law indices are considered, i.e., $n_B = 0.2, 1$, and 1.8, which correspond to shear-thinning, Newtonian, and shear-thickening fluids, respectively. For small Re and Ca, the droplet would eventually deform to an ellipsoidal shape, and the droplet deformation can be quantified by the deformation parameter $D = (L - B)/(L + B)$, where L and B are the lengths of the long and short axes of the ellipsoidal droplet, respectively. Since the pioneering work of Taylor [55], a number of theoretical or phenomenological models [56–58] have been developed to predict the deformation parameter in Newtonian fluid systems. Among them, the MMSH model [58] considers both the wall confinement and the transient effect, and exhibits an excellent prediction accuracy against experiment data. The MMSH model is given by

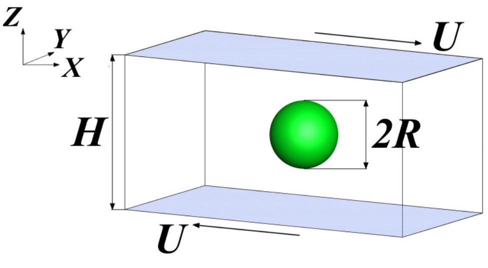

FIG. 3. Illustration of a single droplet in a simple shear flow.

$$D_{\mathrm{MMSH}} = D_{\mathrm{MM}}\left[1 + C_s\frac{1+2.5\lambda}{1+\lambda}\left(\frac{R}{H}\right)^3\right], \tag{30}$$

$$D_{\mathrm{MM}} = \frac{\sqrt{m_1^2 + \mathrm{Ca}^2} - \sqrt{m_1^2 + \left(1 - m_2^2\right)\mathrm{Ca}^2}}{m_2\mathrm{Ca}}, \tag{31}$$

where $\lambda = \mu_R/\mu_B$ is the viscosity ratio, $m_1 = 40(\lambda + 1)/[(2\lambda + 3) \times (19\lambda + 16)]$, $m_2 = [5/(2\lambda + 3)] + [3\mathrm{Ca}^2/(2 + 6\mathrm{Ca}^2)]$, and $64 \times 64 \times 256$ is a shape parameter, which is taken as 5.699 for a droplet placed in the middle of two plates. The MMSH model will be applied to validate our simulation results regarding Newtonian fluid systems and serve as a reference for quantifying the non-Newtonian rheological effects.

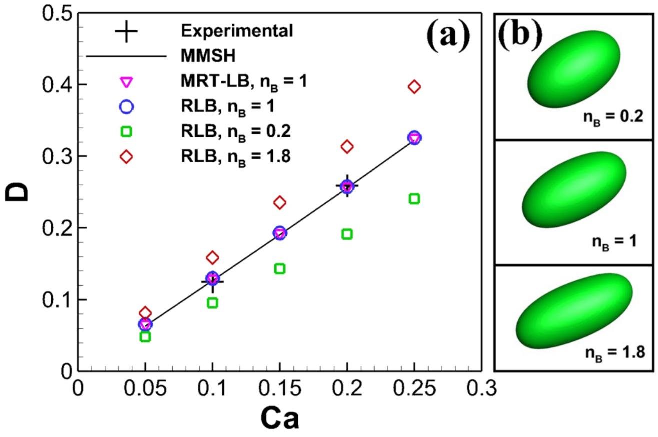

FIG. 4. (a) Deformation parameter D as a function of the capillary number for three different matrix fluids at $\mathrm{Re} = 0.1$, $\lambda = 1$, and $2R/H = 0.5$. The solid line represents the predictions from the MMSH model. The inverted triangles and crosses are both the Newtonian fluid results: the former from the MRT model, and the latter from the experiments of Sibillo *et al.* [60]. (b) Final droplet shapes at $\mathrm{Ca} = 0.25$ for the shear-thinning ($n_B = 0.2$), Newtonian ($n_B = 1$), and shear-thickening ($n_B = 1.8$) matrix fluids.

First, we conduct the simulations on the droplet deformation for $\mathrm{Re} = 0.1$ and $\lambda = 1$ over a range of capillary numbers from 0.05 to 0.25. The domain size is set to be $180 \times 110 \times 80$ with the droplet radius $R = 20$, which were found to produce grid-independent results [39]. Note that only one half domain is used in the y direction due to the symmetry of the problem. The half-way bounce-back scheme [59] is applied on the top and bottom walls, while periodic boundary conditions are imposed in the x and y directions.

Figure 4 plots the deformation parameter D as a function of the capillary number for three different values of n_B, where the predictions from the MMSH model, the experimental data of Sibillo *et al.* in a Newtonian system [60], and the simulated results from the MRT color-gradient model are also plotted for comparison. Note that the MRT color-gradient model for power-law fluids has been presented and well validated in our recent work [39]. It is seen in the Newtonian case ($n_B = 1$) that the deformation parameter obtained by the RLB model exhibits a linear dependence on Ca, and all the results are in good agreement with the MMSH predictions, the experimental data, and the simulated results from the MRT model. This indicates that the present RLB model can provide accurate predictions of the droplet deformation. Consistent with the Newtonian case, the linear dependence of D on Ca is also observed in either shear-thinning or shear-thickening case. However, compared to the Newtonian case, the deformation parameter at each capillary number is bigger in the shear-thickening case ($n_B = 1.8$) but smaller in the shear-thinning case ($n_B = 0.2$). In addition, as illustrated in Fig. 4(b), a larger deformation parameter corresponds to a smaller inclination angle with respect to the horizontal plane, which signifies that the droplet orients more in the flow direction with increasing deformation. These results regarding the power-law fluid systems agree well with our previous findings obtained with the MRT color-gradient model.

TABLE IV. The values of deformation parameter and run time obtained by the RLB and MRT models for a Newtonian droplet in the shear-thinning ($n_B = 0.2$), Newtonian ($n_B = 1$) and shear-thickening ($n_B = 1.8$) matrix fluids at $\mathrm{Re} = 0.1$, $\mathrm{Ca} = 0.1$, $2R/H = 0.5$, and $\lambda = 1$. Note that the run time t_{phy} is the time required for a simulation when reaching $\dot{\gamma}_0 t = 3$. For $n_B = 1$ the predicted value of the deformation parameter from the MMSH model is 0.1268.

Model	n_B	D	t_{phy}/s
RLB	0.2	0.0951	5534.98
MRT	0.2	0.0950	6463.78
RLB	1	0.1293	5490.77
MRT	1	0.1292	6475.79
RLB	1.8	0.1586	5441.84
MRT	1.8	0.1585	6563.96

Like the present RLB model, the MRT model is also known to have better numerical stability and accuracy over the standard BGK model. To further assess the present model, we make a quantitative comparison of the MRT and RLB models in terms of the model accuracy and computing efficiency. The message-passing interface parallelized codes are developed for both models and are applied to 3D simulations of the droplet deformation with $\mathrm{Re} = 0.1$, $\lambda = 1$, $2R/H = 0.5$, and $\mathrm{Ca} = 0.1$ for three different matrix fluids: $n_B = 0.2, 1$, and 1.8. Each of the simulations is run using 60 cores on a High Performance Computing Cluster that consists of 110 computing nodes with each node equipped with 64GB of DDR4 RAM and two Intel Xeon E5-2690 v3 processors. Table IV shows the simulated deformation parameters from the RLB and MRT models, which are almost the same with the difference of around 1×10^{-4} for each n_B. This indicates that the two models are equally accurate in simulating droplet deformation. In addition, we quantify the run time t_{phy} required for a simulation when reaching $\dot{\gamma}_0 t = 3$, which is also listed in Table IV. It is clear that the run time of the present RLB model is always less than that of the MRT model for a constant n_B. Specifically, in contrast to MRT model, the use of RLB model can decrease the run time by 14.4%, 15.2%, and 17.1% for $n_B = 0.2, 1$, and 1.8, respectively. Thus, the present RLB color-gradient model is preferred for the simulation of power-law fluid flows instead of its MRT counterpart.

A number of theoretical, experimental and numerical studies have revealed that when Ca is above a critical value, the droplet won't reach a steady shape but continues to deform and eventually breaks into daughter droplets [61–64]. To capture the droplet breakup, we increase the capillary number and carry out the simulations in a $240 \times 100 \times 80$ lattice domain, which is long enough for the droplet to be stretched freely in the flow direction. The boundary conditions, Re, λ, confinement ratio, and the power-law indices are all kept the same as those in the droplet deformation simulations.

Figure 5 illustrates the simulated results of the present RLB model in three different matrix fluids. In this figure, empty symbols are used in the cases where no droplet breakup is observed, and filled symbols represent binary breakup, where the droplet splits into two daughter droplets. Following this definition, the critical capillary number (Ca_c) lies between the empty and filled symbols in Fig. 5. It is seen in Newtonian

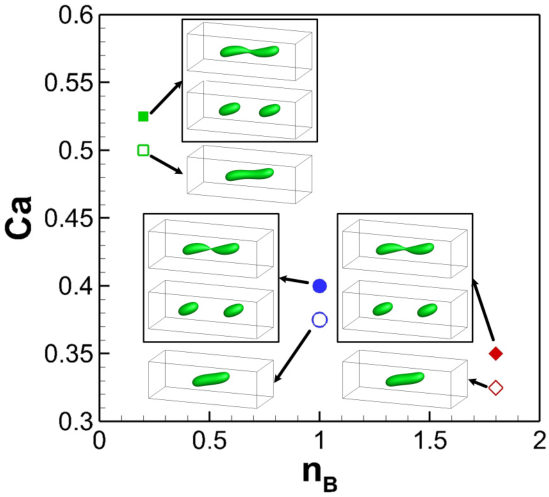

FIG. 5. Capillary numbers at which the droplet achieves a steady shape or experiences breakup for different power-law indices of the matrix fluid. No droplet breakup and binary breakup are represented by empty symbols and filled symbols, respectively. Inset shows either the droplet shapes before and after the breakup or the steady droplet shape.

system that the simulated critical capillary number is in the range of 0.375–0.4, which agrees well with our previous results from the MRT color-gradient model [39]. Note that the present critical capillary number at $n_B = 1$ is a little higher than that obtained by Janssen *et al.* ($\mathrm{Ca}_c = 0.374$) using the boundary integral method [63]; and on the other hand, it is closer to the previous experimental data ($\mathrm{Ca}_c = 0.41$) [63] in comparison with the numerical result of Janssen *et al.* In addition, the values of the critical capillary number are 0.5–0.525 in the shear-thinning matrix fluid ($n_B = 0.2$) and 0.325–0.35 in the shear-thickening matrix fluid ($n_B = 1.8$), suggesting that an increase in power-law index decreases the critical capillary number for droplet breakup. This trend is qualitatively consistent with our previous finding in Ref. [39], where three different power-law indices of $n_B = 0.5, 1$, and 1.5 were considered at various confinement ratios.

IV. CONCLUSIONS

In this work, a regularized lattice Boltzmann color-gradient model is developed to simulate immiscible two-phase flows with power-law rheology. Like the standard BGK color-gradient model, this model uses a forcing term to realize the interfacial tension effect and a recoloring algorithm to produce phase segregation. However, an additional regularization step is introduced prior to the collision step. In the regularization step, the nonequilibrium part of the total distribution function is approximated by its first-order term $f_i^{(1)}$. The constraint equations for $f_i^{(1)}$ are derived using the Chapman-Enskog expansion and are directly solved by the pseudo-inverse method, which does not need prior knowledge about the form of $f_i^{(1)}$ and can be easily extended to other discrete velocity models. The resulting expressions of $f_i^{(1)}$ are related only to macroscopic variables and velocity gradients, which can be evaluated locally. The stability and accuracy of the RLB model are first tested by two benchmark cases with analytical solutions: the single-phase and two-phase power-law fluid flows between two parallel plates. Results show that the present model is capable of simulating power-law fluids with a wide range of power-law indices and has better numerical stability and accuracy over the BGK model. The RLB color-gradient model is then used to simulate the deformation and breakup of a Newtonian droplet in a power-law shear flow. Through quantification of droplet deformation and run time at different power-law indices, the present model is found to have the same accuracy but higher computing efficiency compared to its MRT counterpart. In addition, the critical capillary number for droplet breakup is dependent on the power-law index, and increasing power-law index leads to a decrease in the critical capillary number, consistent with our previous finding in Ref. [39]. The present RLB color-gradient model can offer an accurate and efficient tool for the simulation of non-Newtonian fluid flows and/or Newtonian two-phase flows with high viscosity ratio.

ACKNOWLEDGMENTS

This work is supported by the National Natural Science Foundation of China (Nos. 51506168 and 51711530130), the National Key Research and Development Project of China (No. 2016YFB0200902), the China Postdoctoral Science Foundation (No. 2016M590943), and the Fundamental Research Funds for the Central Universities. H.L. gratefully acknowledges the financial support from Thousand Youth Talents Program for Distinguished Young Scholars and the Young Talent Support Plan of Xi'an Jiaotong University.

APPENDIX A: CHAPMAN-ENSKOG ANALYSIS OF THE RLB MODEL FOR NAVIER-STOKES EQUATIONS

By introducing a regularization step prior to the collision step, the evolution equations of the distribution functions in the RLB color-gradient model are given by

$$f_i(\mathbf{x},t) = f_i^{\mathrm{eq}}(\mathbf{x},t) + f_i^{(1)}(\mathbf{x},t)\delta_t, \tag{A1}$$

$$f_i^{\dagger}(\mathbf{x},t) = f_i(\mathbf{x},t) - \frac{1}{\tau}\left[f_i(\mathbf{x},t) - f_i^{\mathrm{eq}}(\mathbf{x},t)\right] + \hat{F}_i\delta_t, \tag{A2}$$

$$\begin{aligned} f_{i,R}^{\dagger\dagger}(\mathbf{x},t) &= \frac{\rho_R}{\rho} f_i^{\dagger}(\mathbf{x},t) + \beta\frac{\rho_R\rho_B}{\rho}\omega_i\frac{\mathbf{e}_i\cdot\nabla\rho^N}{|\nabla\rho^N|},\\ f_{i,B}^{\dagger\dagger}(\mathbf{x},t) &= \frac{\rho_B}{\rho} f_i^{\dagger}(\mathbf{x},t) - \beta\frac{\rho_R\rho_B}{\rho}\omega_i\frac{\mathbf{e}_i\cdot\nabla\rho^N}{|\nabla\rho^N|}, \end{aligned}\tag{A3}$$

$$f_{i,k}(\mathbf{x}+\mathbf{e}_i\delta_t, t+\delta_t) = f_{i,k}^{\dagger\dagger}(\mathbf{x},t), \quad k = R \text{ or } B, \tag{A4}$$

which are known as the regularization step, BGK collision step, recoloring step, and streaming step, respectively. Note that the forcing term $\hat{F}_i$ is given by Eq. (7). According to the recoloring step, one can get

$$f_{i,R}^{\dagger\dagger}(\mathbf{x},t) + f_{i,B}^{\dagger\dagger}(\mathbf{x},t) = f_i^{\dagger}(\mathbf{x},t). \tag{A5}$$

In addition, from the streaming step, it is easy to obtain

$$\begin{aligned} &f_{i,R}(\mathbf{x}+\mathbf{e}_i\delta_t, t+\delta_t) + f_{i,B}(\mathbf{x}+\mathbf{e}_i\delta_t, t+\delta_t)\\ &\quad = f_{i,R}^{\dagger\dagger}(\mathbf{x},t) + f_{i,B}^{\dagger\dagger}(\mathbf{x},t). \end{aligned}\tag{A6}$$

Using Eq. (A5), Eq. (A6) is further written as

$$f_i(\mathbf{x}+\mathbf{e}_i\delta_t,t+\delta_t) = f_i^{\dagger}(\mathbf{x},t). \tag{A7}$$

Combination of Eqs. (A1), (A2), and (A7) leads to the evolution equation of the total distribution function in the RLB color-gradient model:

$$f_i(\mathbf{x}+\mathbf{e}_i\delta_t,t+\delta_t) - f_i(\mathbf{x},t) = -\frac{1}{\tau} f_i^{(1)}(\mathbf{x},t)\delta_t + \hat{F}_i\delta_t. \tag{A8}$$

It is easily justified that the equilibrium distribution function, defined in Eq. (2), and the forcing term satisfy the following equations:

$$\begin{aligned}
&\sum_i f_i^{\text{eq}} = \rho, \quad \sum_i \mathbf{e}_i f_i^{\text{eq}} = \rho\mathbf{u},\\
&\sum_i \mathbf{e}_i\mathbf{e}_i f_i^{\text{eq}} = \rho\mathbf{u}\mathbf{u} + \rho c_s^2\mathbf{I},\\
&\sum_i \mathbf{e}_{i\alpha}\mathbf{e}_{i\beta}\mathbf{e}_{i\gamma} f_i^{\text{eq}} = \rho c_s^2 \Delta\cdot\mathbf{u}\\
&\qquad = \rho c_s^2(u_\alpha\delta_{\beta\gamma} + u_\beta\delta_{\alpha\gamma} + u_\gamma\delta_{\alpha\beta}),\\
&\sum_i \hat{F}_i = 0, \quad \sum_i \mathbf{e}_i\hat{F}_i = \left(1-\frac{1}{2\tau}\right)\mathbf{F},\\
&\sum_i \mathbf{e}_i\mathbf{e}_i\hat{F}_i = \left(1-\frac{1}{2\tau}\right)(\mathbf{u}\mathbf{F}+\mathbf{F}\mathbf{u}),
\end{aligned} \tag{A9}$$

where the total density and momentum are calculated by

$$\rho = \sum_i f_i, \tag{A10}$$

$$\rho\mathbf{u}(\mathbf{x},t) = \sum_i f_i(\mathbf{x},t)\mathbf{e}_i + \frac{1}{2}\mathbf{F}(\mathbf{x},t)\delta_t. \tag{A11}$$

Applying the Taylor expansion to the left-hand side of Eq. (A8), one can get

$$D_i f_i + \frac{\delta_t}{2} D_i^2 f_i = -\frac{1}{\tau_a}\left(f_i^{(1)}\varepsilon\right) + \hat{F}_i, \tag{A12}$$

where $D_i = \partial t + e_{i\alpha}\partial_\alpha$, and $\tau_a = \tau\delta_t$. Introducing the C-E expansion:

$$\begin{aligned}
f_i &= f_i^{\text{eq}} + \varepsilon f_i^{(1)} + \varepsilon^2 f_i^{(2)} + o(\varepsilon^3),\\
\partial t &= \varepsilon\partial t_0 + \varepsilon^2\partial t_1, \quad \nabla = \varepsilon\nabla_0,\\
\mathbf{F} &= \varepsilon\mathbf{F}^{(0)}, \quad \hat{F}_i = \varepsilon\hat{F}_i^{(0)},
\end{aligned} \tag{A13}$$

where ε is the expansion parameter, and substituting Eq. (A13) into Eq. (A12), we have

$$\begin{aligned}
&(\varepsilon\partial_{t0} + \varepsilon^2\partial_{t1} + \varepsilon\mathbf{e}_i\cdot\nabla_0)\cdot\left[f_i^{\text{eq}} + \varepsilon f_i^{(1)} + \varepsilon^2 f_i^{(2)} + o(\varepsilon^3)\right]\\
&\quad + \frac{\delta_t}{2}(\varepsilon\partial_{t0} + \varepsilon^2\partial_{t1} + \varepsilon\mathbf{e}_i\cdot\nabla_0)^2\\
&\quad \cdot\left[f_i^{\text{eq}} + \varepsilon f_i^{(1)} + \varepsilon^2 f_i^{(2)} + o(\varepsilon^3)\right]\\
&= -\frac{1}{\tau_a}\varepsilon f_i^{(1)} + \varepsilon\hat{F}_i^{(0)}.
\end{aligned} \tag{A14}$$

The following equations can be obtained by matching the terms at different orders of ε:

$$O(\varepsilon): (\partial_{t0} + \mathbf{e}_i\cdot\nabla_0)f_i^{\text{eq}} = -\frac{1}{\tau_a}f_i^{(1)} + \hat{F}_i^{(0)}, \tag{A15}$$

$$O(\varepsilon^2): \partial_{t1}f_i^{\text{eq}} + (\partial_{t0} + \mathbf{e}_i\cdot\nabla_0)f_i^{(1)} + \frac{\delta_t}{2}(\partial_{t0} + \mathbf{e}_i\cdot\nabla_0)^2 f_i^{\text{eq}} = 0. \tag{A16}$$

Substitution of Eq. (A15) into Eq. (A16) leads to

$$\begin{aligned}
&O(\varepsilon^2): \partial_{t1}f_i^{\text{eq}} + (\partial_{t0} + \mathbf{e}_i\cdot\nabla_0)\left[\left(1-\frac{1}{2\tau}\right)f_i^{(1)}\right]\\
&\quad + \frac{\delta_t}{2}(\partial_{t0} + \mathbf{e}_i\cdot\nabla_0)\hat{F}_i^{(0)} = 0.
\end{aligned} \tag{A17}$$

Combining Eqs. (A9)–((A11 and (A13), one can obtain the following solvability conditions for $f_i^{(n)}$ $(n = 1,2,\ldots)$:

$$\begin{aligned}
&\sum_i f_i^{(n)} = 0, \quad n \geqslant 1,\\
&\sum_i \mathbf{e}_{i\alpha} f_i^{(1)} = -\frac{1}{2}F_\alpha^{(0)}\delta_t,\\
&\sum_i \mathbf{e}_i f_i^{(n)} = 0, \quad n > 1.
\end{aligned} \tag{A18}$$

The zeroth and first order moments of Eq. (A15) lead to

$$\partial_{t0}\rho + \nabla_{0\alpha}\cdot(\rho u_\alpha) = 0, \tag{A19}$$

$$\partial_{t0}(\rho u_\alpha) + \nabla_{0\beta}\cdot\left(\rho u_\alpha u_\beta + \rho c_s^2\delta_{\alpha\beta}\right) = F_\alpha^{(0)}. \tag{A20}$$

Similarly, the moments of Eq. (A17) lead to

$$\partial_{t1}\rho = 0, \tag{A21}$$

$$\partial_{t1}(\rho u_\alpha) + \nabla_{0\beta}\cdot\left[\left(1-\frac{1}{2\tau}\right)\sum_i e_{i\alpha}e_{i\beta}f_i^{(1)}\right] + \frac{\delta_t}{2}\nabla_{0\beta}\cdot\left[\left(1-\frac{1}{2\tau}\right)\left(u_\alpha F_\beta^{(0)} + u_\beta F_\alpha^{(0)}\right)\right] = 0, \tag{A22}$$

where the second order tensor $\sum_i e_{i\alpha}e_{i\beta}f_i^{(1)}$ can be calculated by

$$\begin{aligned}
\sum_i \mathbf{e}_i\mathbf{e}_i f_i^{(1)} &= -\tau_a\left[\partial_{t0}\sum_i \mathbf{e}_i\mathbf{e}_i f_i^{\text{eq}} + \nabla_0\cdot\sum_i \mathbf{e}_i\mathbf{e}_i\mathbf{e}_i f_i^{\text{eq}} - \sum_i \mathbf{e}_i\mathbf{e}_i\hat{F}_i^{(0)}\right],\\
&= -\tau_a\left[\partial_{t0}\left(\rho\mathbf{u}\mathbf{u} + \rho c_s^2\mathbf{I}\right) + \nabla_0\cdot\left(\rho c_s^2\Delta\cdot\mathbf{u}\right) - \left(1-\frac{1}{2\tau}\right)(\mathbf{u}\mathbf{F}^{(0)} + \mathbf{F}^{(0)}\mathbf{u})\right].
\end{aligned} \tag{A23}$$

Note that Eq. (A15) has been used in the above derivation.

By virtue of Eqs. (A19) and (A20), the first term on the right-hand side of Eq. (A23) can be written as

$$\begin{aligned}
\partial_{t0}\big(\rho u_\alpha u_\beta + \rho c_s^2\delta_{\alpha\beta}\big) &= \partial_{t0}(\rho u_\alpha u_\beta) - c_s^2\nabla_{0\gamma}\cdot(\rho u_\gamma)\delta_{\alpha\beta}\\
&= u_\beta\partial_{t0}(\rho u_\alpha) + u_\alpha\partial_{t0}(\rho u_\beta) - u_\alpha u_\beta\partial_{t0}(\rho) - c_s^2\nabla_{0\gamma}\cdot(\rho u_\gamma)\delta_{\alpha\beta}\\
&= u_\beta\big[F_\alpha^{(0)} - \nabla_{0\gamma}\cdot\big(\rho u_\alpha u_\gamma + \rho c_s^2\delta_{\alpha\gamma}\big)\big] + u_\alpha\big[F_\beta^{(0)} - \nabla_{0\gamma}\cdot\big(\rho u_\beta u_\gamma + \rho c_s^2\delta_{\gamma\beta}\big)\big]\\
&\quad + u_\alpha u_\beta\nabla_{0\gamma}\cdot(\rho u_\gamma) - c_s^2\nabla_{0\gamma}\cdot(\rho u_\gamma)\delta_{\alpha\beta}\\
&= u_\beta F_\alpha^{(0)} + u_\alpha F_\beta^{(0)} - \nabla_{0\gamma}\cdot(\rho u_\gamma u_\beta u_\alpha) - c_s^2 u_\beta\nabla_{0\alpha}(\rho) - c_s^2 u_\alpha\nabla_{0\beta}(\rho) - c_s^2\nabla_{0\gamma}\cdot(\rho u_\gamma)\delta_{\alpha\beta}.
\end{aligned}\tag{A24}$$

The second term on the right-hand side of Eq. (A23) reads as

$$\begin{aligned}
\nabla_0\cdot\big(\rho c_s^2\Delta\cdot\mathbf{u}\big) &= \nabla_{0\gamma}\big[\rho c_s^2(u_\alpha\delta_{\beta\gamma} + u_\beta\delta_{\alpha\gamma} + u_\gamma\delta_{\alpha\beta})\big],\\
&= c_s^2\nabla_{0\gamma}(\rho u_\gamma)\delta_{\alpha\beta} + \nabla_{0\beta}\big(\rho c_s^2 u_\alpha\big) + \nabla_{0\alpha}\big(\rho c_s^2 u_\beta\big),\\
&= c_s^2\nabla_{0\gamma}(\rho u_\gamma)\delta_{\alpha\beta} + \rho c_s^2\nabla_{0\beta}(u_\alpha) + u_\alpha c_s^2\nabla_{0\beta}(\rho) + \rho c_s^2\nabla_{0\alpha}(u_\beta) + u_\beta c_s^2\nabla_{0\alpha}(\rho).
\end{aligned}\tag{A25}$$

Then Eq. (A23) becomes

$$\begin{aligned}
\sum_i e_{i\alpha}e_{i\beta}f_i^{(1)} &= -\tau_a\left[\rho c_s^2\nabla_{0\beta}(u_\alpha) + \rho c_s^2\nabla_{0\alpha}(u_\beta) - \nabla_{0\gamma}\cdot(\rho u_\gamma u_\beta u_\alpha) + \frac{1}{2\tau}\big(u_\beta F_\alpha^{(0)} + u_\alpha F_\beta^{(0)}\big)\right]\\
&= -\tau_a\rho c_s^2(\nabla_0\mathbf{u} + \nabla_0\mathbf{u}^T) - \frac{\delta_t}{2}(\mathbf{u}\mathbf{F}^{(0)} + \mathbf{F}^{(0)}\mathbf{u}) + o(u^3).
\end{aligned}\tag{A26}$$

Substituting Eq. (A26) into Eq. (A22), we have

$$\begin{aligned}
&\partial_{t1}(\rho u_\alpha) + \nabla_0\cdot\left\{\left(1-\frac{1}{2\tau}\right)\left[-\tau_a\rho c_s^2(\nabla_0\mathbf{u} + \nabla_0\mathbf{u}^T) - \frac{\delta_t}{2}(\mathbf{u}\mathbf{F}^{(0)} + \mathbf{F}^{(0)}\mathbf{u})\right]\right\} + \frac{\delta_t}{2}\nabla_0\cdot\left[\left(1-\frac{1}{2\tau}\right)(\mathbf{u}\mathbf{F}^{(0)} + \mathbf{F}^{(0)}\mathbf{u})\right] = 0;\\
&\Rightarrow \partial_{t1}(\rho u_\alpha) = \nabla_0\cdot\left[\left(\tau - \frac{1}{2}\right)\rho c_s^2(\nabla_0\mathbf{u} + \nabla_0\mathbf{u}^T)\right]\delta_t.
\end{aligned}\tag{A27}$$

Through the calculations of $\varepsilon\times$ Eq. (A19) + $\varepsilon^2\times$ Eq. (A21) and $\varepsilon\times$ Eq. (A20) + $\varepsilon^2\times$ Eq. (A27), the target Navier-Stokes equations [Eq. (12)] can be recovered exactly with the pressure and fluid viscosity given by $p = \rho c_s^2$ and $\mu = c_s^2\delta_t(\tau - 0.5)$, respectively.

APPENDIX B: DESCRIPTION ON HOW TO COMPUTE NONEQUILIBRIUM PART OF DISTRIBUTION FUNCTION

In this appendix, we take the D2Q9 lattice as an example to describe how to compute the nonequilibrium part $f_i^{(1)}$ from Eq. (19).

First, Eq. (19) can be expressed in a matrix form as $\mathbf{A}\mathbf{f}^{(1)} = \mathbf{b}$, where

$$\mathbf{A} = \begin{pmatrix}
1 & 1 & 1 & 1 & 1 & 1 & 1 & 1 & 1\\
0 & 1 & 0 & -1 & 0 & 1 & -1 & -1 & 1\\
0 & 0 & 1 & 0 & -1 & 1 & 1 & -1 & -1\\
0 & 1 & 0 & 1 & 0 & 1 & 1 & 1 & 1\\
0 & 0 & 0 & 0 & 0 & 1 & -1 & 1 & -1\\
0 & 0 & 1 & 0 & 1 & 1 & 1 & 1 & 1
\end{pmatrix},\tag{B1}$$

$$\mathbf{b} = \big(0 \quad -\tfrac{1}{2}F_x \quad -\tfrac{1}{2}F_y \quad \eta S_{xx} \quad \eta S_{xy} \quad \eta S_{yy}\big)^T,\tag{B2}$$

$$\mathbf{f}^{(1)} = \big(f_0^{(1)}\ f_1^{(1)}\ f_2^{(1)}\ f_3^{(1)}\ f_4^{(1)}\ f_5^{(1)}\ f_6^{(1)}\ f_7^{(1)}\ f_8^{(1)}\big)^T.\tag{B3}$$

Then, following Campbell and Meyer [51], the pseudo-inverse of $\mathbf{A}$ is given by

$$\mathbf{A}^{-1} = \mathbf{A}^T(\mathbf{A}\mathbf{A}^T)^{-1} = \frac{1}{36}\begin{pmatrix}
20 & 0 & 0 & -12 & 0 & -12\\
8 & 6 & 0 & 6 & 0 & -12\\
8 & 0 & 6 & -12 & 0 & 6\\
8 & 6 & 0 & 6 & 0 & -12\\
8 & 0 & -6 & -12 & 0 & 6\\
-4 & 6 & 6 & 6 & 9 & 6\\
-4 & -6 & 6 & 6 & -9 & 6\\
-4 & -6 & -6 & 6 & 9 & 6\\
-4 & 6 & -6 & 6 & -9 & 6
\end{pmatrix},\tag{B4}$$

where $\mathbf{A}^T$ and $\mathbf{A}^{-1}$ denote the transport and inverse of a matrix $\mathbf{A}$, respectively.

Finally, $\mathbf{f}^{(1)}$ is calculated by

$$\mathbf{f}^{(1)} = \mathbf{A}^{-1}\mathbf{b} = \frac{1}{36}\begin{pmatrix} 20 & 0 & 0 & -12 & 0 & -12 \\ 8 & 6 & 0 & 6 & 0 & -12 \\ 8 & 0 & 6 & -12 & 0 & 6 \\ 8 & 6 & 0 & 6 & 0 & -12 \\ 8 & 0 & -6 & -12 & 0 & 6 \\ -4 & 6 & 6 & 6 & 9 & 6 \\ -4 & -6 & 6 & 6 & -9 & 6 \\ -4 & -6 & -6 & 6 & 9 & 6 \\ -4 & 6 & -6 & 6 & -9 & 6 \end{pmatrix}\begin{pmatrix} 0 \\ -\frac{1}{2}F_x \\ -\frac{1}{2}F_y \\ \eta S_{xx} \\ \eta S_{xy} \\ \eta S_{yy} \end{pmatrix} = \frac{1}{36}\begin{pmatrix} 0 & 0 & -12 & 0 & -12 \\ -3 & 0 & 6 & 0 & -12 \\ 0 & -3 & -12 & 0 & 6 \\ 3 & 0 & 6 & 0 & -12 \\ 0 & 3 & -12 & 0 & 6 \\ -3 & -3 & 6 & 9 & 6 \\ 3 & -3 & 6 & -9 & 6 \\ 3 & 3 & 6 & 9 & 6 \\ -3 & 3 & 6 & -9 & 6 \end{pmatrix}\begin{pmatrix} F_x \\ F_y \\ \eta S_{xx} \\ \eta S_{xy} \\ \eta S_{yy} \end{pmatrix}. \quad \text{(B5)}$$

---

[1] Q. Li, K. Luo, Q. Kang, Y. He, Q. Chen, and Q. Liu, Lattice Boltzmann methods for multiphase flow and phase-change heat transfer, Prog. Energy Combust. Sci. **52**, 62 (2016).

[2] A. Ferrari, J. Jimenez-Martinez, T. L. Borgne, Y. Méheust, and I. Lunati, Challenges in modeling unstable two-phase flow experiments in porous micromodels, Water Resour. Res. **51**, 1381 (2015).

[3] H. Başağaoğlu, J. R. Harwell, H. Nguyen, and S. Succi, Enhanced computational performance of the lattice Boltzmann model for simulating micron- and submicron-size particle flows and non-Newtonian fluid flows, Comput. Phys. Commun. **213**, 64 (2017).

[4] N. Wang, H. Liu, and C. Zhang, Three-dimensional phase-field lattice Boltzmann model for incompressible multiphase flows, J. Comput. Sci. **17**, 340 (2016).

[5] X. He and L.-S. Luo, *A priori* derivation of the lattice Boltzmann equation, Phys. Rev. E **55**, R6333(R) (1997).

[6] S. Chen and G. D. Doolen, Lattice Boltzmann method for fluid flows, Annu. Rev. Fluid Mech. **30**, 329 (1998).

[7] X. Shan and H. Chen, Lattice Boltzmann model for simulating flows with multiple phases and components, Phys. Rev. E **47**, 1815 (1993).

[8] T. Lee and C.-L. Lin, A stable discretization of the lattice Boltzmann equation for simulation of incompressible two-phase flows at high density ratio, J. Comput. Phys. **206**, 16 (2005).

[9] Y. Wang, C. Shu, H. Huang, and C. Teo, Multiphase lattice Boltzmann flux solver for incompressible multiphase flows with large density ratio, J. Comput. Phys. **280**, 404 (2015).

[10] M. Sbragaglia, R. Benzi, L. Biferale, S. Succi, K. Sugiyama, and F. Toschi, Generalized lattice Boltzmann method with multirange pseudopotential, Phys. Rev. E **75**, 026702 (2007).

[11] A. Fakhari and D. Bolster, Diffuse interface modeling of three-phase contact line dynamics on curved boundaries: A lattice Boltzmann model for large density and viscosity ratios, J. Comput. Phys. **334**, 620 (2017).

[12] C. K. Aidun and J. R. Clausen, Lattice-Boltzmann method for complex flows, Annu. Rev. Fluid Mech. **42**, 439 (2010).

[13] H. Huang, J.-J. Huang, and X.-Y. Lu, A mass-conserving axisymmetric multiphase lattice Boltzmann method and its application in simulation of bubble rising, J. Comput. Phys. **269**, 386 (2014).

[14] P. L. Bhatnagar, E. P. Gross, and M. Krook, A model for collision processes in gases. I. Small amplitude processes in charged and neutral one-component systems, Phys. Rev. **94**, 511 (1954).

[15] Y. Qian, D. d'Humières, and P. Lallemand, Lattice BGK models for Navier-Stokes equation, Europhys. Lett. **17**, 479 (1992).

[16] D. d'Humières, Generalized lattice-Boltzmann equations, in *Rarefied Gas Dynamics: Theory and Simulations*, edited by D. P. Weaver and B. D. Shizgal, Progress in Astronautics and Aeronautics (AIAA, Reston, VA, 1992), Vol. 159, pp. 450–458.

[17] I. Ginzburg and D. d'Humières, Multireflection boundary conditions for lattice Boltzmann models, Phys. Rev. E **68**, 066614 (2003).

[18] L.-S. Luo, W. Liao, X. Chen, Y. Peng, and W. Zhang, Numerics of the lattice Boltzmann method: Effects of collision models on the lattice Boltzmann simulations, Phys. Rev. E **83**, 056710 (2011).

[19] S. Chikatamarla, S. Ansumali, and I. Karlin, Entropic Lattice Boltzmann Models for Hydrodynamics in Three Dimensions, Phys. Rev. Lett. **97**, 010201 (2006).

[20] I. Karlin, F. Bösch, and S. Chikatamarla, Gibbs' principle for the lattice-kinetic theory of fluid dynamics, Phys. Rev. E **90**, 031302 (2014).

[21] I. Karlin, A. Ferrante, and H. Öttinger, Perfect entropy functions of the lattice Boltzmann method, Europhys. Lett. **47**, 182 (1999).

[22] J. Latt and B. Chopard, Lattice Boltzmann method with regularized pre-collision distribution functions, Math. Comput. Simul. **72**, 165 (2006).

[23] H. Chen, R. Zhang, I. Staroselsky, and M. Jhon, Recovery of full rotational invariance in lattice Boltzmann formulations for high Knudsen number flows, Physica A **362**, 125 (2006).

[24] R. Zhang, X. Shan, and H. Chen, Efficient kinetic method for fluid simulation beyond the Navier-Stokes equation, Phys. Rev. E **74**, 046703 (2006).

[25] A. Montessori, G. Falcucci, P. Prestininzi, M. La Rocca, and S. Succi, Regularized lattice Bhatnagar-Gross-Krook model for two- and three-dimensional cavity flow simulations, Phys. Rev. E **89**, 053317 (2014).

[26] A. Mazloomi Moqaddam, S. S. Chikatamarla, and I. V. Karlin, Simulation of binary droplet collisions with the entropic lattice Boltzmann method, Phys. Fluids **28**, 022106 (2016).

[27] M. Izham, T. Fukui, and K. Morinishi, A comparative study of regularized lattice Boltzmann method and entropic lattice

Boltzmann method for high Reynolds number flow, in *The Asian Symposium on Computational Heat Transfer and Fluid Flow, ASCHT2011, Kyoto, Japan* (2011), p. 63.

[28] F. Higuera, S. Succi, and R. Benzi, Lattice gas dynamics with enhanced collisions, Europhys. Lett. **9**, 345 (1989).

[29] K. K. Mattila, P. C. Philippi, and L. A. Hegele Jr., High-order regularization in lattice-Boltzmann equations, Phys. Fluids **29**, 046103 (2017).

[30] M. Basha and C. S. Nor Azwadi, Regularized lattice Boltzmann simulation of laminar mixed convection in the entrance region of 2-D channels, Numer. Heat Transf. A **63**, 867 (2013).

[31] O. Malaspinas, Increasing stability and accuracy of the lattice Boltzmann scheme: Recursivity and regularization, arXiv:1505.06900.

[32] L. Wang, Z. Chai, and B. Shi, Regularized lattice Boltzmann simulation of double-diffusive convection of power-law nanofluids in rectangular enclosures, Int. J. Heat. Mass Transf. **102**, 381 (2016).

[33] L. Wang, B. Shi, and Z. Chai, Regularized lattice Boltzmann model for a class of convection-diffusion equations, Phys. Rev. E **92**, 043311 (2015).

[34] H. Otomo, H. Fan, R. Hazlett, Y. Li, I. Staroselsky, R. Zhang, and H. Chen, Simulation of residual oil displacement in a sinusoidal channel with the lattice Boltzmann method, C. R. Mec. **343**, 559 (2015).

[35] H. Otomo, H. Fan, Y. Li, M. Dressler, I. Staroselsky, R. Zhang, and H. Chen, Studies of accurate multi-component lattice Boltzmann models on benchmark cases required for engineering applications, J. Comput. Sci. **17**, 334 (2016).

[36] Q. Li, K. Luo, and X. Li, Forcing scheme in pseudopotential lattice Boltzmann model for multiphase flows, Phys. Rev. E **86**, 016709 (2012).

[37] S. Dhinakaran, M. Oliveira, F. Pinho, and M. Alves, Steady flow of power-law fluids in a 1:3 planar sudden expansion, J. Non-Newton. Fluid Mech. **198**, 48 (2013).

[38] Q. Li, N. Hong, B. Shi, and Z. Chai, Simulation of power-law fluid flows in two-dimensional square cavity using multi-relaxation-time lattice Boltzmann method, Commun. Comput. Phys. **15**, 265 (2014).

[39] N. Wang, H. Liu, and C. Zhang, Deformation and breakup of a confined droplet in shear flows with power-law rheology, J. Rheol. **61**, 741 (2017).

[40] I. Halliday, R. Law, C. Care, and A. Hollis, Improved simulation of drop dynamics in a shear flow at low Reynolds and capillary number, Phys. Rev. E **73**, 056708 (2006).

[41] I. Halliday, A. Hollis, and C. Care, Lattice Boltzmann algorithm for continuum multicomponent flow, Phys. Rev. E **76**, 026708 (2007).

[42] J. Brackbill, D. B. Kothe, and C. Zemach, A continuum method for modeling surface tension, J. Comput. Phys. **100**, 335 (1992).

[43] Z. Guo, C. Zheng, and B. Shi, Discrete lattice effects on the forcing term in the lattice Boltzmann method, Phys. Rev. E **65**, 046308 (2002).

[44] H. Liu, Y. Ju, N. Wang, G. Xi, and Y. Zhang, Lattice Boltzmann modeling of contact angle and its hysteresis in two-phase flow with large viscosity difference, Phys. Rev. E **92**, 033306 (2015).

[45] Y. Zu and S. He, Phase-field-based lattice Boltzmann model for incompressible binary fluid systems with density and viscosity contrasts, Phys. Rev. E **87**, 043301 (2013).

[46] A. K. Gunstensen, D. H. Rothman, S. Zaleski, and G. Zanetti, Lattice Boltzmann model of immiscible fluids, Phys. Rev. A **43**, 4320 (1991).

[47] M. Latva-Kokko and D. H. Rothman, Diffusion properties of gradient-based lattice Boltzmann models of immiscible fluids, Phys. Rev. E **71**, 056702 (2005).

[48] H. Liu, A. J. Valocchi, and Q. Kang, Three-dimensional lattice Boltzmann model for immiscible two-phase flow simulations, Phys. Rev. E **85**, 046309 (2012).

[49] X. Shan, X.-F. Yuan, and H. Chen, Kinetic theory representation of hydrodynamics: A way beyond the Navier-Stokes equation, J. Fluid Mech. **550**, 413 (2006).

[50] L. Jódar, A. Law, A. Rezazadeh, J. Weston, and G. Wu, Computations for the Moore Penrose and other generalized inverses, Congressus Numerantium **80**, 57 (1991).

[51] S. L. Campbell and C. D. Meyer, *Generalized Inverses of Linear Transformations* (SIAM, Philadelphia, 2009).

[52] Z. Chai, B. Shi, Z. Guo, and F. Rong, Multiple-relaxation-time lattice Boltzmann model for generalized Newtonian fluid flows, J. Non-Newton. Fluid Mech. **166**, 332 (2011).

[53] R. Cardinaels, S. Afkhami, Y. Renardy, and P. Moldenaers, An experimental and numerical investigation of the dynamics of microconfined droplets in systems with one viscoelastic phase, J. Non-Newton. Fluid Mech. **166**, 52 (2011).

[54] M. Favelukis and A. Nir, Non-Newtonian slender drops in a simple shear flow, J. Non-Newton. Fluid Mech. **228**, 38 (2016).

[55] G. Taylor, The formation of emulsions in definable fields of flow, Proc. R. Soc. Lond. Ser. A **146**, 501 (1934).

[56] M. Shapira and S. Haber, Low Reynolds number motion of a droplet in shear flow including wall effects, Int. J. Multiphas. Flow **16**, 305 (1990).

[57] P. Maffettone and M. Minale, Equation of change for ellipsoidal drops in viscous flow, J. Non-Newton. Fluid Mech. **78**, 227 (1998).

[58] A. Vananroye, P. Van Puyvelde, and P. Moldenaers, Effect of confinement on the steady-state behavior of single droplets during shear flow, J. Rheol. **51**, 139 (2007).

[59] A. J. Ladd, Numerical simulations of particulate suspensions via a discretized Boltzmann equation. Part 1. Theoretical foundation, J. Fluid Mech. **271**, 285 (1994).

[60] V. Sibillo, G. Pasquariello, M. Simeone, V. Cristini, and S. Guido, Drop Deformation in Microconfined Shear Flow, Phys. Rev. Lett. **97**, 054502 (2006).

[61] R. Cardinaels, A. Vananroye, P. Van Puyvelde, and P. Moldenaers, Breakup criteria for confined droplets: Effects of compatibilization and component viscoelasticity, Macromol. Mater. Eng. **296**, 214 (2011).

[62] E. Chiarello, A. Gupta, G. Mistura, M. Sbragaglia, and M. Pierno, Droplet breakup driven by shear thinning solutions in a microfluidic T-junction, Phys. Rev. Fluids **2**, 123602 (2017).

[63] P. Janssen, A. Vananroye, P. Van Puyvelde, P. Moldenaers, and P. Anderson, Generalized behavior of the breakup of viscous drops in confinements, J. Rheol. **54**, 1047 (2010).

[64] H. A. Stone, Dynamics of drop deformation and breakup in viscous fluids, Annu. Rev. Fluid Mech. **26**, 65 (1994).